Science Advances
AAAS

Supplementary Materials for

Structure of the human TSC:WIPI3 lysosomal recruitment complex

Charles Bayly-Jones *et al.*

Corresponding author: Andrew M. Ellisdon, andrew.ellisdon@monash.edu

Sci. Adv. **10**, eadr5807 (2024)
DOI: 10.1126/sciadv.adr5807

This PDF file includes:

Figs. S1 to S10
Tables S1 and S2
References

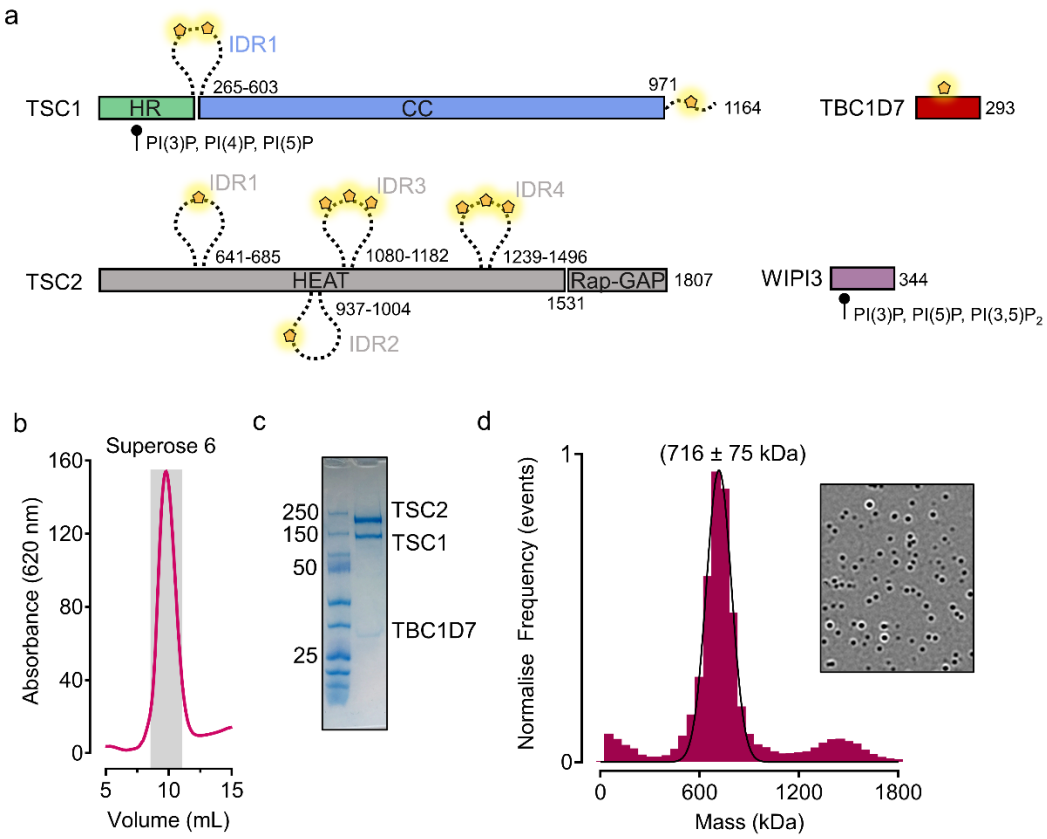

Fig. S1. Recombinant TSC production and characterisation

(**A**) Primary domain structure schematic illustrating large intrinsically disordered loops (IDRs), approximate regions of phosphorylation (yellow star), and PIP binding sites. (**B**) Size exclusion chromatography profile of human TSC (Superose 6, Cytiva) and (**C**) corresponding Coomassie-stained SDS-PAGE. (**D**) Single-molecule mass frequency distribution of recombinant TSC measured by mass photometry landing assay. Inset, representative mass-contrast difference image.

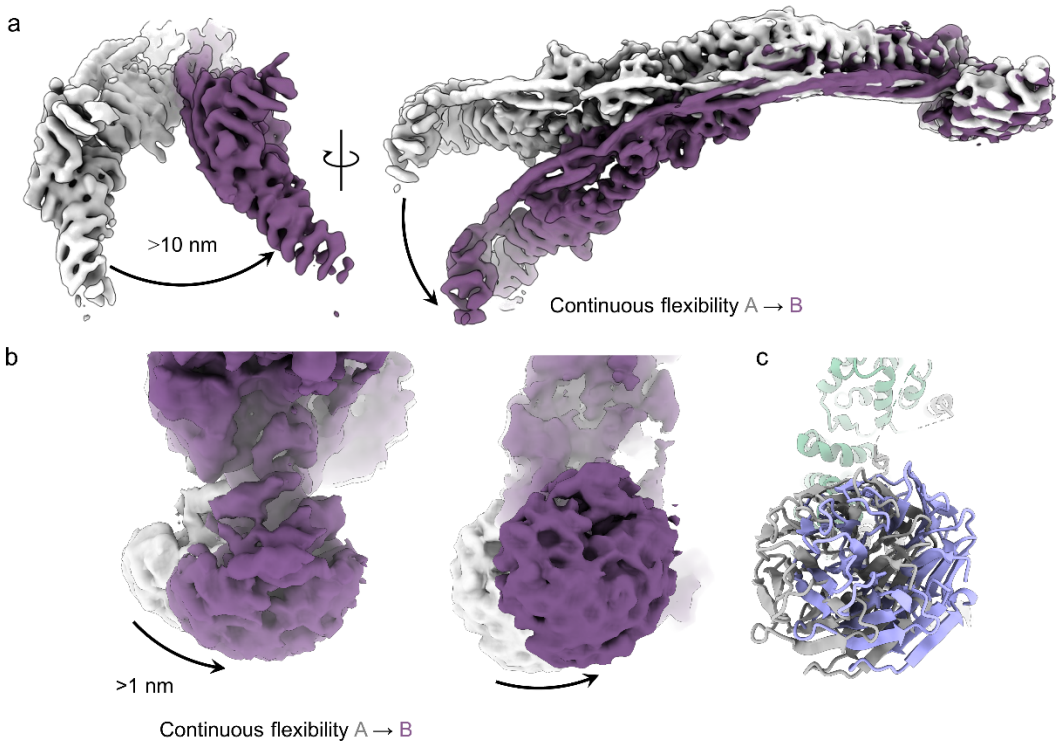

Fig. S2. TSC is highly flexible and undergoes continuous conformational dynamics.

(**A**) To visualize the extent of flexibility across the whole composite map, we performed cryoSPARC 3D variational analysis (3DVA) (*59*) on each focused refinement. Extrema from along the length of the complex were matched and joined into two composite maps. The resultant maps were superimposed based on the TSC1 N-terminal dimer. Two extrema of the observed continuous conformational characteristics of TSC are shown. Differences of as much as 100 Å are possible. (**B**) WIPI3 undergoes a pivoting motion about the anchor site of TSC1. These motions are on the order of 10 Å. Two extrema are shown (left: purple, grey), with cartoon rendering (right). (**C**) Ribbon representation of (B).

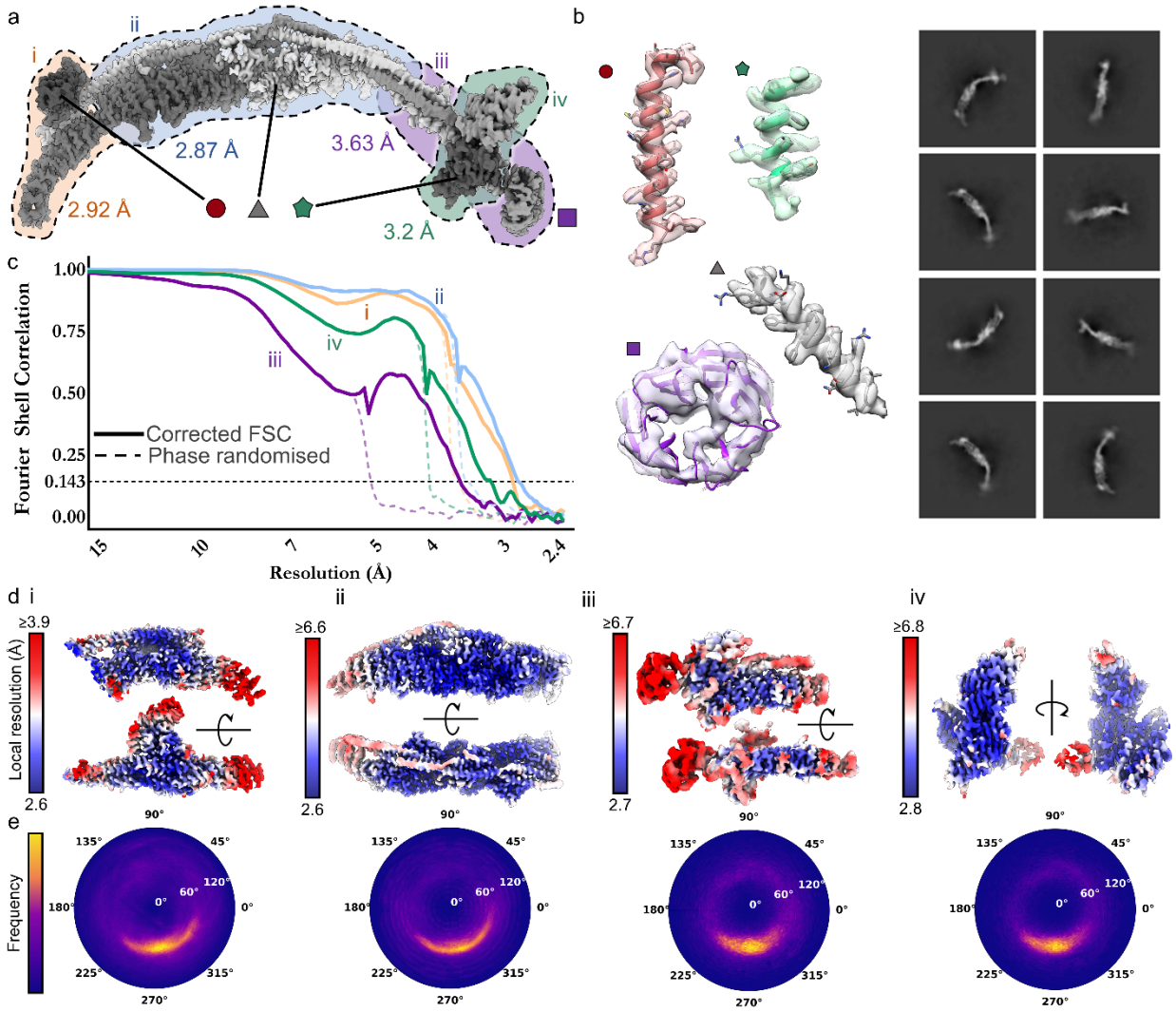

Fig. S3. Single particle cryo-EM analysis and validation

(**A**) Composite reconstruction of TSC with approximate regions used for focused refinements. (**B**) Select regions corresponding to the shape-key from (A) of high resolution cryo-EM density and corresponding model. The WIPI3 local resolution suffers due to conformational dynamics. (**C**) Half-map Fourier shell correlation curve reveals resolution estimates for each focused refinement (I to IV). Continuous conformational dynamics of WIPI3 (see iii) likely account for the observed reduction in correlation in the frequency range of 10 to 4 Å. (**D**) Variation of local resolution across each focused refinement. High resolution features corresponding to 2.6 Å are present in the core and TBC1D7 regions. Lower resolution of 2.8 Å is present in the core of the N-terminal TSC1 dimer domain and the WIPI3 focused refinement. **e.** Angular distribution plot in polar coordinates, frequency of assigned particle orientation parameters is shown as a heat map (Center to edge, tilt angle. Circumference, azimuthal angle).

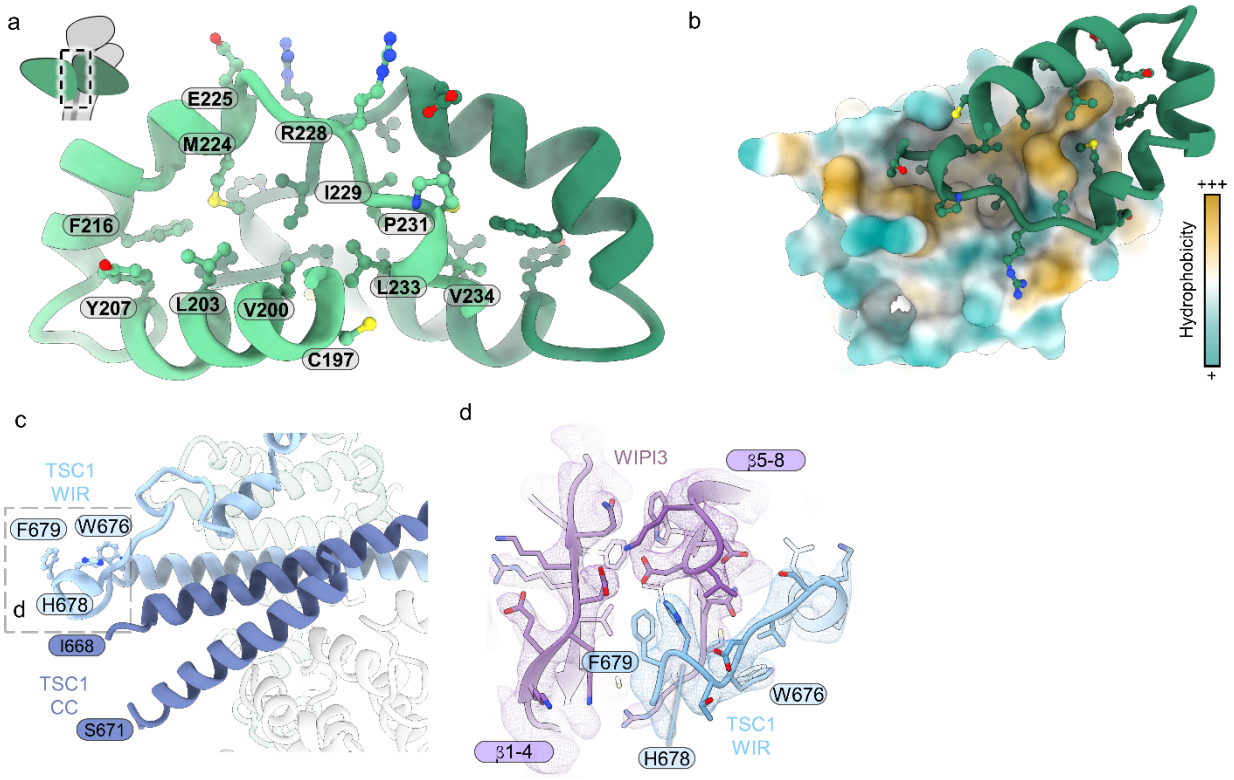

Fig. S4. The TSC N-terminal HR dimer interface.

(**A**) Residues 197 to 234 of TSC1 define a symmetrical interface of the dimer domain. Key residues that mediate this interaction are predominantly hydrophobic. A pair of intermolecular salt bridges are defined by R228 and E225 from both TSC1 copies. (**B**) The dimer interface rendered as a surface, colored by degree of hydrophobicity. A natural knobs-into-holes conformation is present which mediates the major contacts between each TSC1 chain. (**C**) The TSC1 coiled-coil (CC) is asymmetrically organized proximal to WIPI3. (**D**) Focused electron density of the TSC1 (light blue) and WIPI3 (purple) interaction, illustrating the key TSC1 interface residues F679, H678, and W676 (2Fo-Fc electron density map contoured at 1.0 σ).

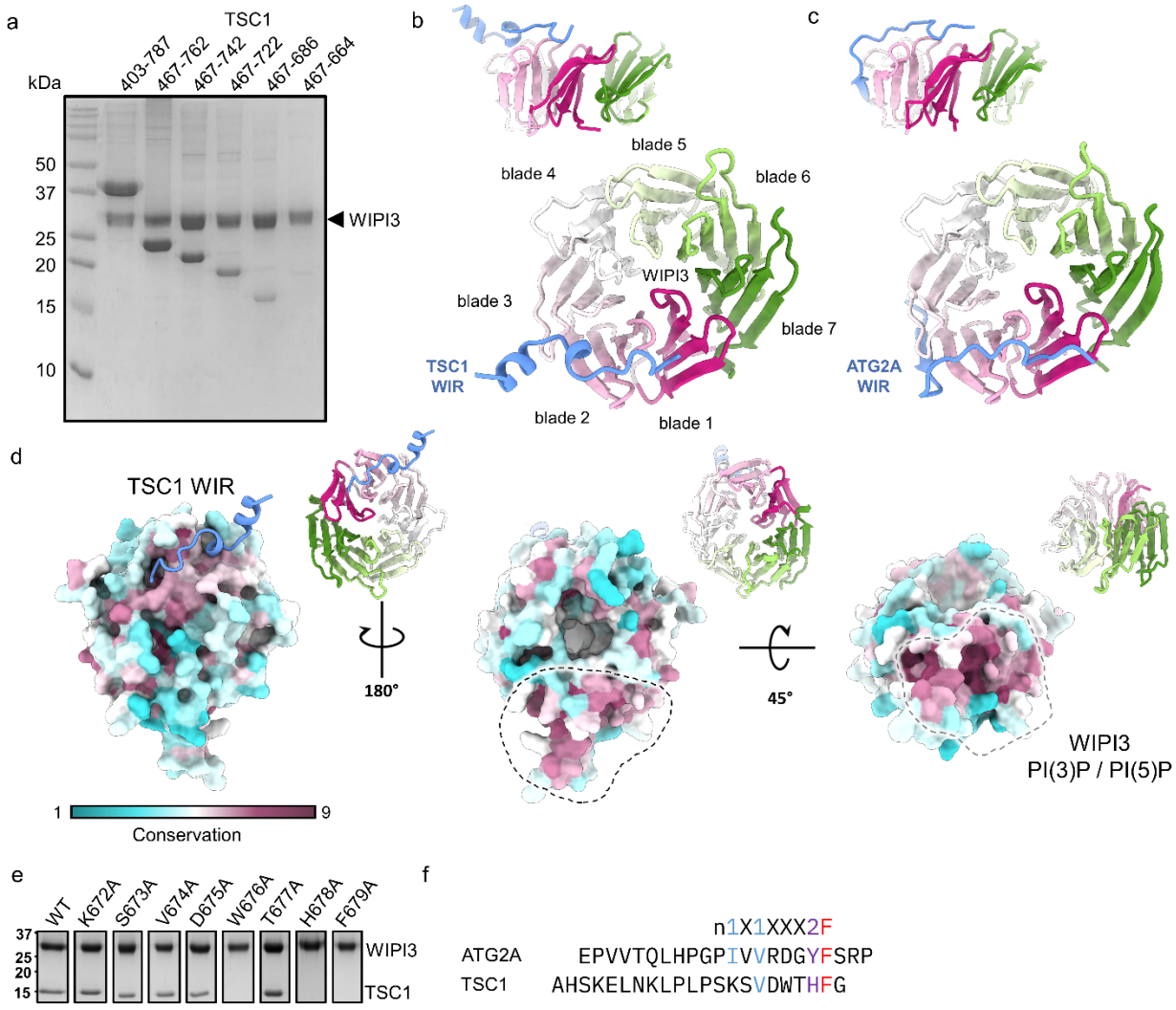

Fig. S5. Comparison between TSC1:WIPI3 and ATG2A:WIPI3 WIR motifs.

(**A**) Coomassie stained 15 % (w/v) SDS-polyacrylamide gel of TSC1 truncation constructs and WIPI3. (**B**) The crystal structure of TSC1:WIPI3. (**C**) The crystal structure of ATG2A:WIPI3 (*25*) rendered as in (B). TSC1 and ATG2A WIR motifs bind WIPI3 between blade 2 and 3, with additional contacts from the motif occurring along the surface of blade 1. These data suggest that TSC and ATG2A may compete for WIPI3 binding within the cell. However, the WIPI4:ATG2A interaction, rather than WIPI3:ATG2A, appears central to the role ATG2As in autophagosome formation (*60*). As such, it is unclear whether TSC and ATG2A competition for WIPI3 binding has a key biological role. (**D**) Surface conservation of WIPI3 highlights the WIR binding pocket is conserved in WIPI3, as is the PIP-binding sites between blade 5 and 6. (**E**) Alanine scan and Ni-NTA chromatography pulldown assay of WIPI3 and indicated mutant TSC1 fragments (residues 467-685, Δ500-603). (**F**) Sequence alignment of the canonical WIR motif of ATG2A and TSC1.

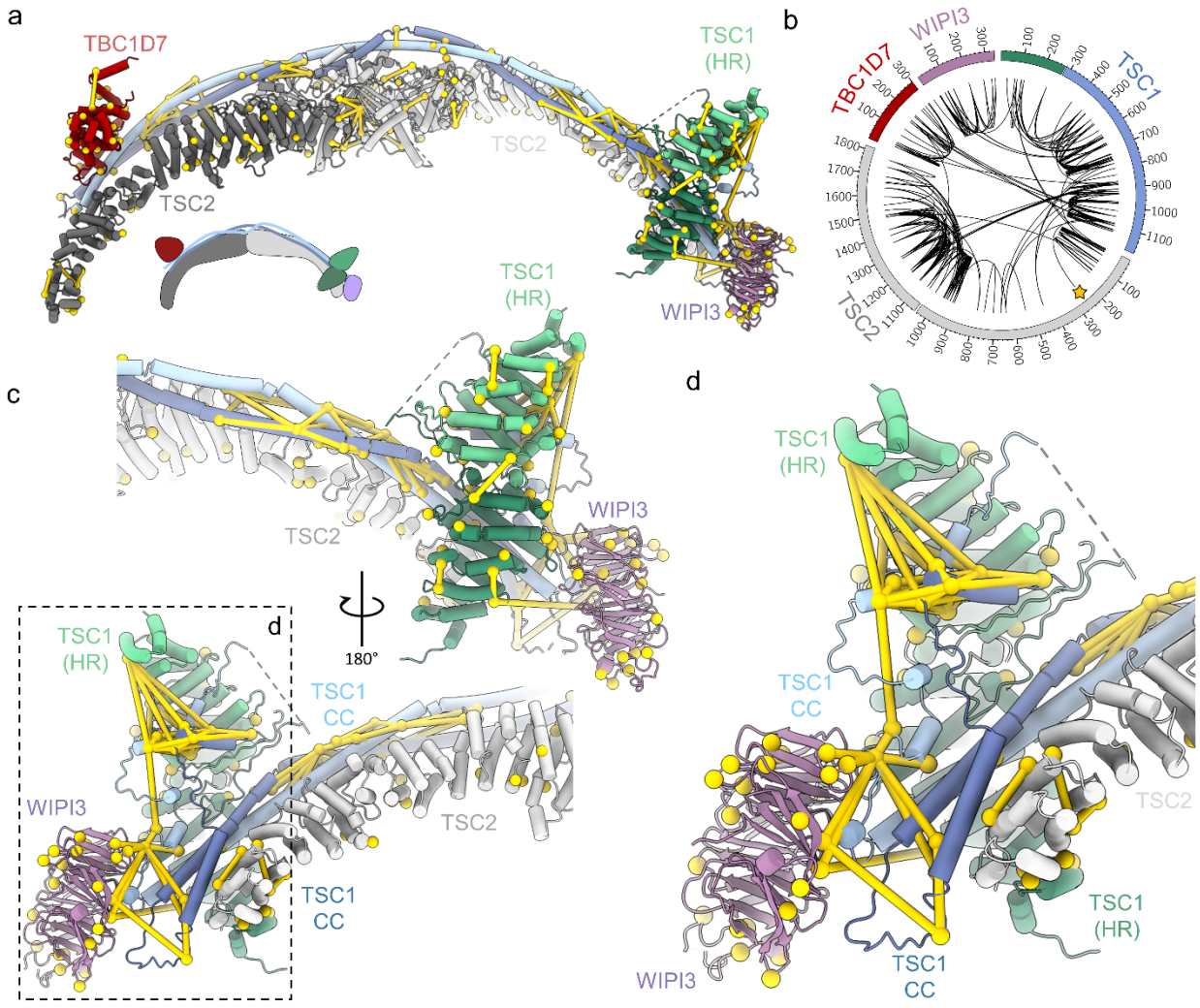

Fig. S6. Cross-linking mass spectrometry of the TSC:WIPI3 complex.

(**A**) Cartoon overview of the full TSC:WIPI3 model. BS^3 cross-link distance restraints are shown as yellow pseudobonds. Lysine Cβ atoms are shown as yellow spheres. We identified six unique distance constraints between WIPI3 and the TSC1 coil-coil domain that strongly agree with the cryo-EM and crystal structures. Further, extensive intermolecular cross-linking constraints map across the TSC1 coil-coil dimer and the TSC2 HEAT and Rap-GAP domains. Lastly, close inspection of the TSC1 N-terminal HR domains showed numerous cross-links consistent with the TSC HR dimer model and its TSC1 coiled-coil interaction, including intermolecular interface cross-links between a lysine pair within the TSC1 HR domain (K238). (**B**) Domain and component layout of TSC with Circos plot of cross-linking data from (A). Long- and short-range cross-links are visible. A cross-link between the unresolved region of the TSC1 C-terminus and the TSC2 N-terminus is highlighted (yellow star), suggesting further long-range contacts. (**C**) Focused view of the TSC1 HR dimer and WIPI3 regions. (**D**) Boxed region from (C) showing key cross-linking constraints confirming the placement of WIPI3 relative to TSC. Cross-links are also observed between the local structured regions of the TSC1 extended loop (IDR1).

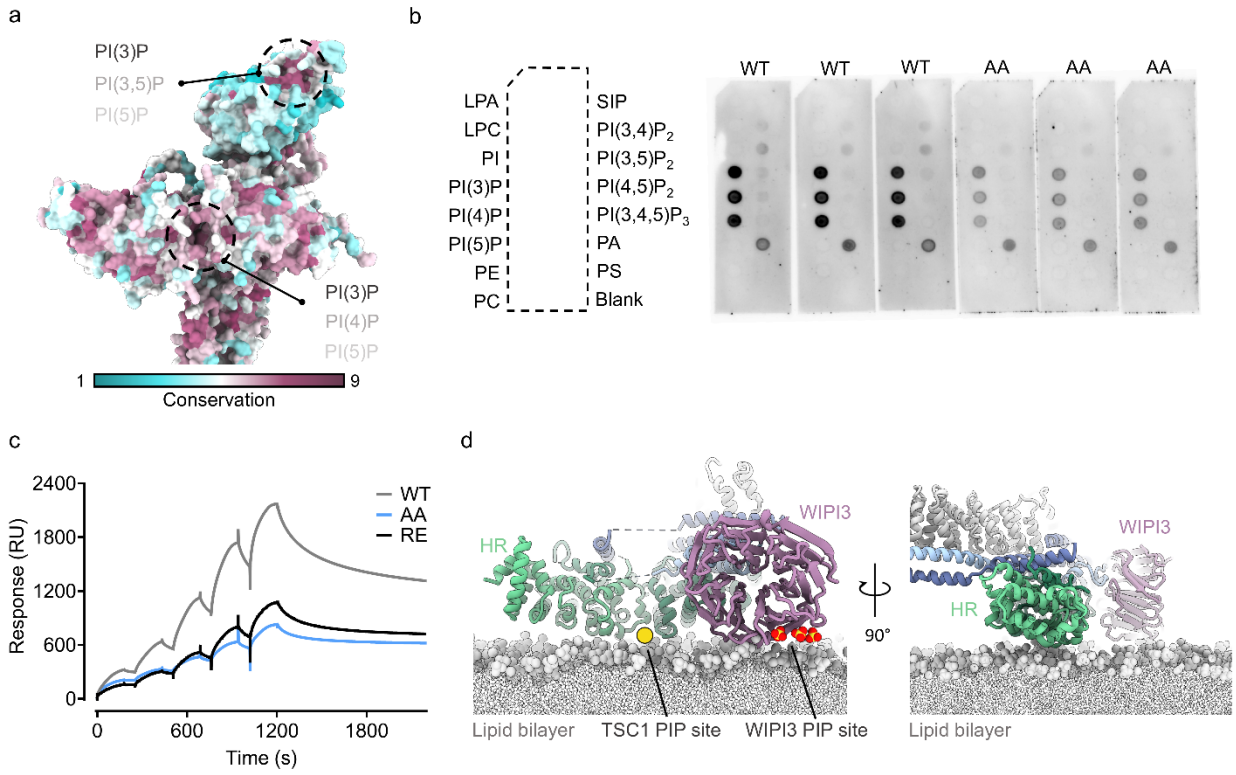

Fig. S7. TSC interactions with monophosphorylated phosphatidylinositol.

(**A**) Surface rendering coloured by residue conservation (higher is more conserved). PIP binding sites are visible as strongly conserved pockets (indicated by dashed circles) that correlate with positively charged regions from (Fig. 3b). (**B**) Replicate phosphatidylinositol lipid membrane strips. WT, wild type. AA, TSC K238A, R204A. (**C**) Example surface plasmon resonance single-cycle sensorgrams of wild-type TSC, TSC K238A R304A (AA), and TSC R204E (RE). Mechanical artefacts at injection points have been excluded for clarity. RU, response units. The R_{MAX} is dependent on the level of ligand (PI(3)P) on the chip surface, the analyte (TSC) and ligand (PI(3)P) molecular weights, and the number of binding sites. Direct comparisons between TSC WT and TSC mutants were undertaken under conditions whereby all variables other than the number of binding sites were constant. For each experimental repeat, we consistently observed a notable drop in the R_{MAX} value consistent with the loss of a PI(3)P binding site upon TSC1 HR mutation. (**D**) Cartoon rendering of the TSC:WIPI3 complex docked against a planar lipid bilayer. The TSC1 HR and WIPI3 PIP binding sites are flush with the lipid bilayer plane thereby defining a flat interaction surface.

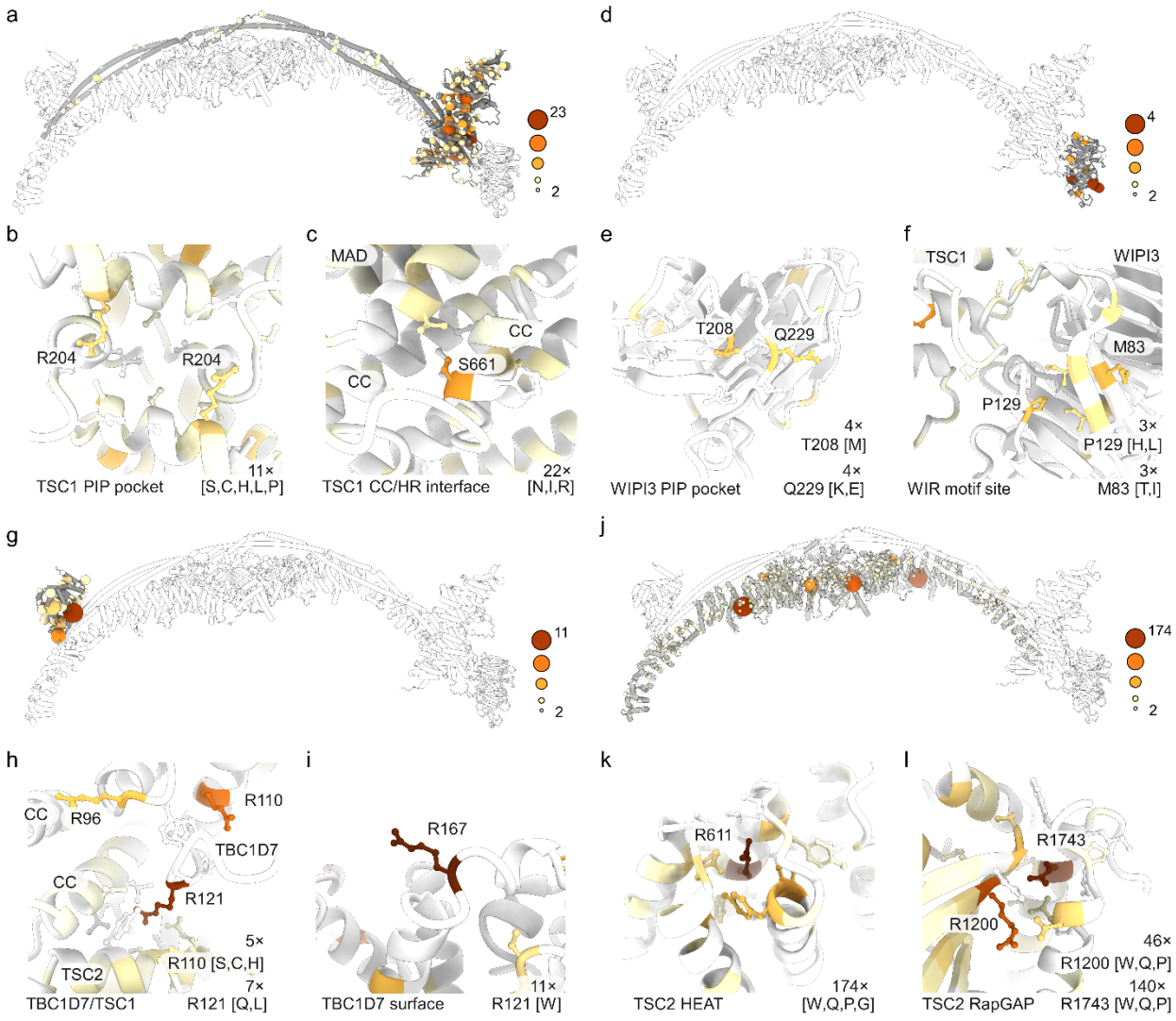

Fig. S8. Disease-associated TSC mutations.

(**A**) TSC1 shown as pipes and planks with disease-associated mutations rendered as spheres, other components are shown as white silhouettes. A clear mutational hotspot in TSC1 is clustered to the TSC1 HR dimer. (**B**) Central arginine residues of the TSC HR dimer PIP pocket are one of the most frequently observed TSC1 mutations. (**C**) Highly mutated S661 is located at the TSC1 CC/HR interface. (**D**) WIPI3 rendered as in (A). The most frequent WIPI3 mutations cluster to the PIP binding pocket of WIPI3. (**E**) Residues T208 and Q229 of the PIP pocket are highlighted. (**F**) The TSC1 WIR binding pocket (blade 2) of WIPI3 possesses several frequently mutated residues, potentially affecting local protein folding. (**G**) TBC1D7 mutations cluster to the TSC1:TBC1D7 interface. (**H**) A triplet of arginine residues, R96, R110, and R121 at the TBC1D7:TSC1 interface are frequently mutated and associated with disease. (**I**) A surface exposed arginine is, somewhat surprisingly, the most frequent disease-associated missense mutation in TBC1D7. The functional outcome of this mutation is currently unclear. (**J**) The core of TSC2 possesses a high frequency of mutations, with two key residues, R611 and R1743 being mutated as many as 174 and 140 times, respectively. (**K**) The buried R611 residue of TSC2 within the HEAT repeats, is the most frequently mutated TSC residue despite not being located in the central Rap-GAP domain or TSC

core. (**L**) Several residues of key importance to the TSC2 Rap-GAP domain are observed owing to their high frequency of loss-of-function disease-associated mutation.

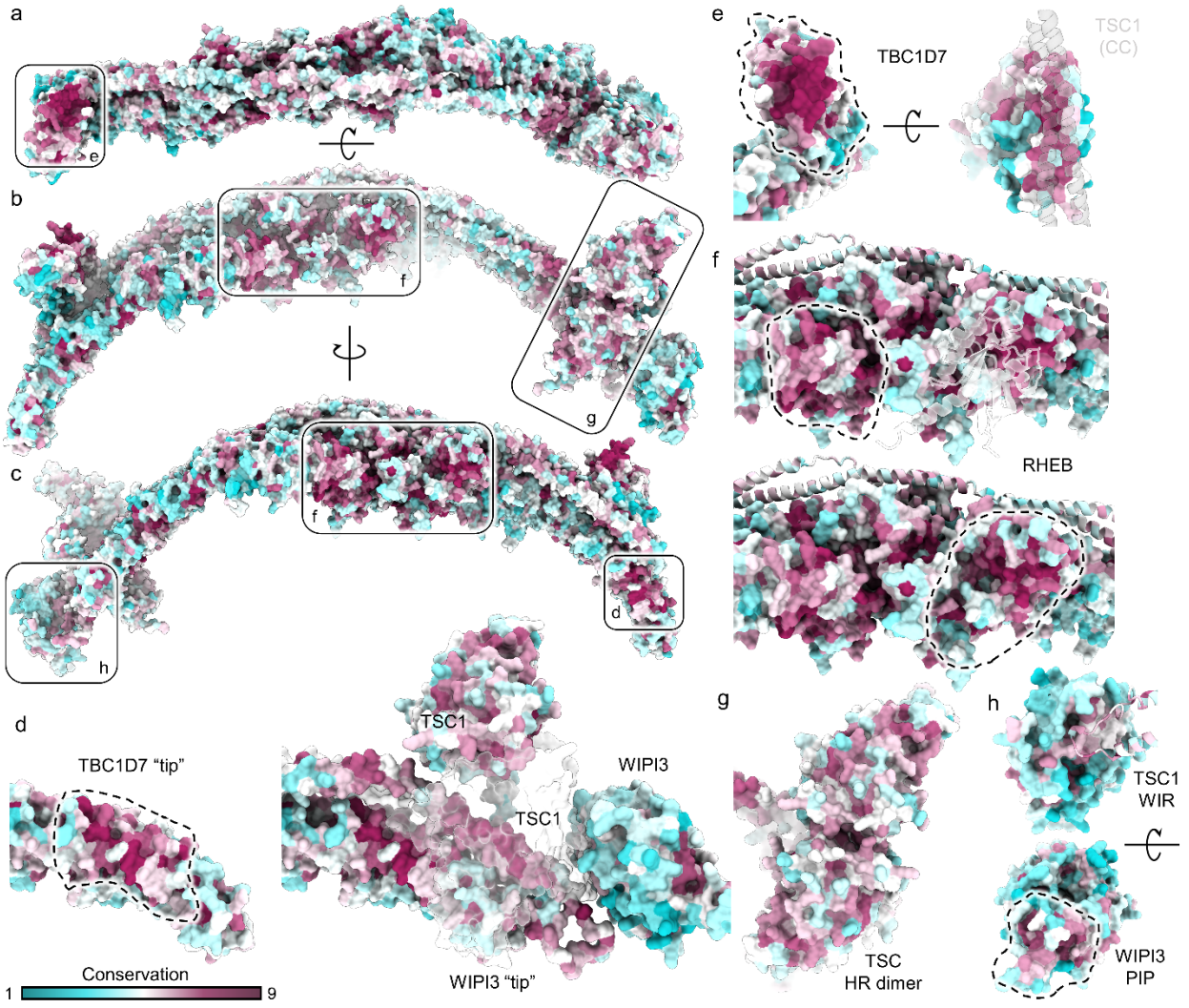

Fig. S9. Complex-wide surface conservation of the complete TSC.

(**A**) Top-down view and (**B**), side view of TSC showing the central core RHEB binding interface (F) and the TSC1 N-terminal dimer domain (G). (**C**) Side view of TSC rotated 180° relative to (B). The WIPI3 interface is boxed (H) and a region of high surface conservation is highlighted (D). (**D**) Two views of the conserved region from (C). A single copy of TSC1 is shown as a transparent white surface. The surface of the TSC2 N-terminus is conserved, this relates to the requirement of the symmetrically related region to mediate the TSC1 N-terminal domain clamp and interface. (**E**) The exposed surface of TBC1D7 is very strongly conserved, as is the underside (left) which mediates TSC1 (transparent ribbon) interactions. (**F**) Two key sites of conservation are present in the TSC2 central core. A region of unknown functional significance is highly conserved (top; RHEB shown as transparent cartoon). Proximal to this unknown site, is the RHEB binding site (bottom; dashed region). Both sites are conserved to a similar extent. (**G**) Focused view of the TSC1 N-terminal dimer highlighting extensive surface conservation along the modelled membrane binding interface and the recessed PIP-binding pocket. (**H**) The WIPI3 subunit shows two regions of surface conservation, corresponding to the known WIR motif and PIP binding pockets, consistent with their key functional roles.

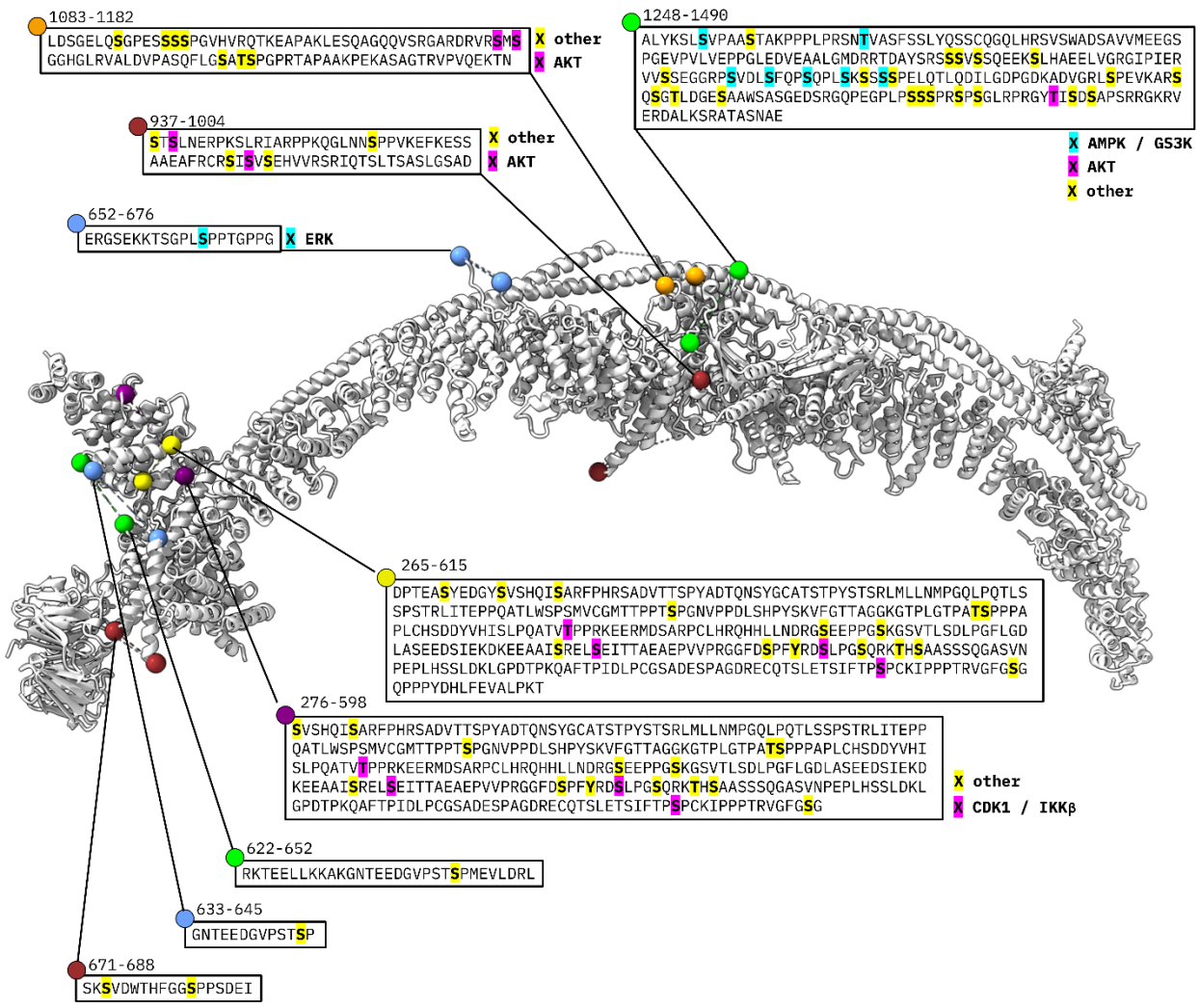

Fig. S10. TSC intrinsically disordered loops are the targets of phosphorylation.

The exit and entry points of unresolved, large intrinsically disordered loops are shown and colored as spheres. The amino acid sequences corresponding to these loops are shown, phosphorylation sites are highlighted and are in bold font.

Table S1.
Cryo-EM data collection, refinement, and validation statistics

	Whole TSC (EMD 45492) (PDB 9CE3) composite	Whole TSC (EMD 45510) consensus	Core (EMD 45511) focused	TSC1 HR dimer (EMD 45112) focused	TBC1D7 (EMD 45113) focused	TBCD17/TSC2 (EMD 45514) focused	WIPI3 (EMD 45515) focused	WIPI3/TSC2 (EMD 45529) focused
Data collection and processing								
Magnification	105,000	105,000	105,000	105,000	105,000	105,000	105,000	105,000
Voltage (kV)	300	300	300	300	300	300	300	300
Electron exposure (e^{-}/Å^2)	46.54	46.54	46.54	46.54	46.54	46.54	46.54	46.54
Defocus range (μm)	−1.4 ± 0.7	−1.4 ± 0.7	−1.4 ± 0.7	−1.4 ± 0.7	−1.4 ± 0.7	−1.4 ± 0.7	−1.4 ± 0.7	−1.4 ± 0.7
Pixel size (Å)	0.8234	0.8234	0.8234	0.8234	0.8234	0.8234	0.8234	0.8234
Symmetry imposed	C1	C1	C1	C1	C1	C1	C1	C1
Initial particle images (no.)	Composite	1,176,292	1,176,292	1,176,292	1,176,292	1,176,292	1,176,292	1,176,292
Final particle images (no.)	Composite	84487	415,120	99,927	542,899	542899	112,945	112945
Map resolution (Å) 0.143 FSC threshold	~2.8*	3.45	2.87	3.29	2.93	2.96	3.62	3.77
Map resolution range (Å)	2.6-6.0	3.34-12.0	2.6−6.6	2.8−6.8	2.6−3.9	2.6−3.9	2.7−6.7	2.7−6.7
Refinement								
Initial model used (PDB code)	De novo, 9C91, 5EJC							
Model resolution (Å) 0.5 FSC threshold	3.1							
Map sharpening *B* factor (Å^2)	N/A							
Model composition								
Non-hydrogen atoms	35095							
Protein residues	4379							
B factors (Å^2)	87.05							
R.M.S. deviations								
Bond lengths (Å)	0.008							
Bond angles (°)	1.446							
Validation								
MolProbity score	1.21							
Clashscore	2.55							
Poor rotamers (%)	0.61							
Ramachandran plot								
Favored (%)	97.00							
Allowed (%)	3.00							
Disallowed (%)	0.00							

*Global resolution estimated by Fourier shell correlation of two half-map composites, see Materials and Methods.

Table S2.
Data collection and refinement statistics

	TSC1:WIPI3 (PDB 9C9I)
Data collection	
Space group	$P4_1$
Cell dimensions	
a, *b*, *c* (Å)	94.241, 94.241, 199.386
α, β, γ (°)	90, 90, 90
Resolution (Å)	47.12-3.17 (3.37-3.17)*
R_{merge}	0.242 (2.857)
R_{pim}	0.067 (0.797)
$I / \sigma I$	11.1 (1.1)
$CC_{1/2}$	0.997 (0.376)
Completeness (%)	98.9 (93.4)
Redundancy	13.9 (13.1)
Refinement	
Resolution (Å)	47.06-3.181
No. reflections	28780
R_{work} / R_{free}	0.1975/0.2549
No. atoms	10118
Protein	10118
Ligand/ion	0
Water	0
B-factors	108.21
Protein	108.21
Ligand/ion	0
Water	0
R.m.s. deviations	
Bond lengths (Å)	0.002
Bond angles (°)	0.43

*A single crystal was used for the structure.

*Values in parentheses are for highest-resolution shell.

REFERENCES AND NOTES

1. M. Laplante, D. M. Sabatini, mTOR signaling in growth control and disease. *Cell* **149**, 274–293 (2012).

2. Y. Zhang, X. Gao, L. J. Saucedo, B. Ru, B. A. Edgar, D. Pan, Rheb is a direct target of the tuberous sclerosis tumour suppressor proteins. *Nat. Cell Biol.* **5**, 578–581 (2003).

3. K. Inoki, Y. Li, T. Xu, K. L. Guan, Rheb GTPase is a direct target of TSC2 GAP activity and regulates mTOR signaling. *Genes Dev.* **17**, 1829–1834 (2003).

4. A. R. Tee, B. D. Manning, P. P. Roux, L. C. Cantley, J. Blenis, Tuberous sclerosis complex gene products, Tuberin and Hamartin, control mTOR signaling by acting as a GTPase-activating protein complex toward Rheb. *Curr. Biol.* **13**, 1259–1268 (2003).

5. A. F. Castro, J. F. Rebhun, G. J. Clark, L. A. Quilliam, Rheb binds tuberous sclerosis complex 2 (TSC2) and promotes S6 kinase activation in a rapamycin- and farnesylation-dependent manner. *J. Biol. Chem.* **278**, 32493–32496 (2003).

6. R. V. Duran, M. N. Hall, Regulation of TOR by small GTPases. *EMBO Rep.* **13**, 121–128 (2012).

7. C. C. Dibble, W. Elis, S. Menon, W. Qin, J. Klekota, J. M. Asara, P. M. Finan, D. J. Kwiatkowski, L. O. Murphy, B. D. Manning, TBC1D7 is a third subunit of the TSC1-TSC2 complex upstream of mTORC1. *Mol. Cell* **47**, 535–546 (2012).

8. E. P. Henske, S. Jozwiak, J. C. Kingswood, J. R. Sampson, E. A. Thiele, Tuberous sclerosis complex. *Nat. Rev. Dis. Primers.* **2**, 16035 (2016).

9. J. Huang, B. D. Manning, The TSC1-TSC2 complex: A molecular switchboard controlling cell growth. *Biochem. J.* **412**, 179–190 (2008).

10. K. Inoki, H. Ouyang, T. Zhu, C. Lindvall, Y. Wang, X. Zhang, Q. Yang, C. Bennett, Y. Harada, K. Stankunas, C. Y. Wang, X. He, O. A. MacDougald, M. You, B. O. Williams, K. L.

Guan, TSC2 integrates Wnt and energy signals via a coordinated phosphorylation by AMPK and GSK3 to regulate cell growth. *Cell* **126**, 955–968 (2006).

11. K. Inoki, T. Zhu, K. L. Guan, TSC2 mediates cellular energy response to control cell growth and survival. *Cell* **115**, 577–590 (2003).

12. L. Ma, Z. Chen, H. Erdjument-Bromage, P. Tempst, P. P. Pandolfi, Phosphorylation and functional inactivation of TSC2 by Erk implications for tuberous sclerosis and cancer pathogenesis. *Cell* **121**, 179–193 (2005).

13. P. P. Roux, B. A. Ballif, R. Anjum, S. P. Gygi, J. Blenis, Tumor-promoting phorbol esters and activated Ras inactivate the tuberous sclerosis tumor suppressor complex via p90 ribosomal S6 kinase. *Proc. Natl. Acad. Sci. U.S.A.* **101**, 13489–13494 (2004).

14. B. D. Manning, A. R. Tee, M. N. Logsdon, J. Blenis, L. C. Cantley, Identification of the tuberous sclerosis complex-2 tumor suppressor gene product tuberin as a target of the phosphoinositide 3-kinase/akt pathway. *Mol. Cell* **10**, 151–162 (2002).

15. K. Inoki, Y. Li, T. Zhu, J. Wu, K. L. Guan, TSC2 is phosphorylated and inhibited by Akt and suppresses mTOR signalling. *Nat. Cell Biol.* **4**, 648–657 (2002).

16. C. J. Potter, L. G. Pedraza, T. Xu, Akt regulates growth by directly phosphorylating Tsc2. *Nat. Cell Biol.* **4**, 658–665 (2002).

17. D. Bakula, A. J. Muller, T. Zuleger, Z. Takacs, M. Franz-Wachtel, A. K. Thost, D. Brigger, M. P. Tschan, T. Frickey, H. Robenek, B. Macek, T. Proikas-Cezanne, WIPI3 and WIPI4 β-propellers are scaffolds for LKB1-AMPK-TSC signalling circuits in the control of autophagy. *Nat. Commun.* **8**, 15637 (2017).

18. C. Demetriades, N. Doumpas, A. A. Teleman, Regulation of TORC1 in response to amino acid starvation via lysosomal recruitment of TSC2. *Cell* **156**, 786–799 (2014).

19. S. Yang, Y. Zhang, C. Y. Ting, L. Bettedi, K. Kim, E. Ghaniam, M. A. Lilly, The Rag GTPase regulates the dynamic behavior of TSC downstream of both amino acid and growth factor restriction. *Dev. Cell* **55**, 272–288.e5 (2020).

20. M. T. Prentzell, U. Rehbein, M. C. Sandoval, A. S. De Meulemeester, R. Baumeister, L. Brohee, B. Berdel, M. Bockwoldt, B. Carroll, S. R. Chowdhury, A. von Deimling, C. Demetriades, G. Figlia; Genomics England Research Consortium, M. E. G. de Araujo, A. M. Heberle, I. Heiland, B. Holzwarth, L. A. Huber, J. Jaworski, M. Kedra, K. Kern, A. Kopach, V. I. Korolchuk, I. van 't Land-Kuper, M. Macias, M. Nellist, W. Palm, S. Pusch, J. M. R. Pittol, M. Reil, A. Reintjes, F. Reuter, J. R. Sampson, C. Scheldeman, A. Siekierska, E. Stefan, A. A. Teleman, L. E. Thomas, O. Torres-Quesada, S. Trump, H. D. West, P. de Witte, S. Woltering, T. E. Yordanov, J. Zmorzynska, C. A. Opitz, K. Thedieck, G3BPs tether the TSC complex to lysosomes and suppress mTORC1 signaling. *Cell* **184**, 655–674.e27 (2021).

21. H. Yang, Z. Yu, X. Chen, J. Li, N. Li, J. Cheng, N. Gao, H. X. Yuan, D. Ye, K. L. Guan, Y. Xu, Structural insights into TSC complex assembly and GAP activity on Rheb. *Nat. Commun.* **12**, 339 (2021).

22. K. Ramlaul, W. Fu, H. Li, N. de Martin Garrido, L. He, M. Trivedi, W. Cui, C. H. S. Aylett, G. Wu, Architecture of the tuberous sclerosis protein complex. *J. Mol. Biol.* **433**, 166743 (2021).

23. K. Fitzian, A. Bruckner, L. Brohee, R. Zech, C. Antoni, S. Kiontke, R. Gasper, A. L. Linard Matos, S. Beel, S. Wilhelm, V. Gerke, C. Ungermann, M. Nellist, S. Raunser, C. Demetriades, A. Oeckinghaus, D. Kummel, TSC1 binding to lysosomal PIPs is required for TSC complex translocation and mTORC1 regulation. *Mol. Cell* **81**, 2705–2721.e8 (2021).

24. D. L. Dai, S. M. N. Hasan, G. Woollard, Y. M. Abbas, S. A. Bueler, J. P. Julien, J. L. Rubinstein, M. T. Mazhab-Jafari, Structural characterization of endogenous tuberous sclerosis protein complex revealed potential polymeric assembly. *Biochemistry* **60**, 1808–1821 (2021).

25. J. Ren, R. Liang, W. Wang, D. Zhang, L. Yu, W. Feng, Multi-site-mediated entwining of the linear WIR-motif around WIPI beta-propellers for autophagy. *Nat. Commun.* **11**, 2702 (2020).

26. M. Ebner, D. Puchkov, O. Lopez-Ortega, P. Muthukottiappan, Y. Su, C. Schmied, S. Zillmann, I. Nikonenko, J. Koddebusch, G. L. Dornan, M. T. Lucht, V. Koka, W. Jang, P. A.

Koch, A. Wallroth, M. Lehmann, B. Brugger, M. Pende, D. Winter, V. Haucke, Nutrient-regulated control of lysosome function by signaling lipid conversion. *Cell* **186**, 5328–5346. e26 (2023).

27. Y. Posor, W. Jang, V. Haucke, Phosphoinositides as membrane organizers. *Nat. Rev. Mol. Cell Biol.* **23**, 797–816 (2022).

28. S. Baskaran, M. J. Ragusa, E. Boura, J. H. Hurley, Two-site recognition of phosphatidylinositol 3-phosphate by PROPPINs in autophagy. *Mol. Cell* **47**, 339–348 (2012).

29. R. Liang, J. Ren, Y. Zhang, W. Feng, Structural conservation of the two phosphoinositide-binding sites in WIPI proteins. *J. Mol. Biol.* **431**, 1494–1505 (2019).

30. S. Schrotter, C. J. Yuskaitis, M. R. MacArthur, S. J. Mitchell, A. M. Hosios, M. Osipovich, M. E. Torrence, J. R. Mitchell, G. Hoxhaj, M. Sahin, B. D. Manning, The non-essential TSC complex component TBC1D7 restricts tissue mTORC1 signaling and brain and neuron growth. *Cell Rep.* **39**, 110824 (2022).

31. S. Q. Zheng, E. Palovcak, J. P. Armache, K. A. Verba, Y. Cheng, D. A. Agard, MotionCor2: Anisotropic correction of beam-induced motion for improved cryo-electron microscopy. *Nat. Methods* **14**, 331–332 (2017).

32. A. Rohou, N. Grigorieff, CTFFIND4: Fast and accurate defocus estimation from electron micrographs. *J. Struct. Biol.* **192**, 216–221 (2015).

33. A. Punjani, J. L. Rubinstein, D. J. Fleet, M. A. Brubaker, cryoSPARC: Algorithms for rapid unsupervised cryo-EM structure determination. *Nat. Methods* **14**, 290–296 (2017).

34. T. Bepler, A. Morin, M. Rapp, J. Brasch, L. Shapiro, A. J. Noble, B. Berger, Positive-unlabeled convolutional neural networks for particle picking in cryo-electron micrographs. *Nat. Methods* **16**, 1153–1160 (2019).

35. T. Wagner, F. Merino, M. Stabrin, T. Moriya, C. Antoni, A. Apelbaum, P. Hagel, O. Sitsel, T. Raisch, D. Prumbaum, D. Quentin, D. Roderer, S. Tacke, B. Siebolds, E. Schubert, T. R.

Shaikh, P. Lill, C. Gatsogiannis, S. Raunser, SPHIRE-crYOLO is a fast and accurate fully automated particle picker for cryo-EM. *Commun. Biol.* **2**, 218 (2019).

36. J. Zivanov, T. Nakane, B. O. Forsberg, D. Kimanius, W. J. Hagen, E. Lindahl, S. H. Scheres, New tools for automated high-resolution cryo-EM structure determination in RELION-3. *eLife* **7**, e42166 (2018).

37. G. Tang, L. Peng, P. R. Baldwin, D. S. Mann, W. Jiang, I. Rees, S. J. Ludtke, EMAN2: An extensible image processing suite for electron microscopy. *J. Struct. Biol.* **157**, 38–46 (2007).

38. R. Sanchez-Garcia, J. Gomez-Blanco, A. Cuervo, J. M. Carazo, C. O. S. Sorzano, J. Vargas, DeepEMhancer: A deep learning solution for cryo-EM volume post-processing. *Commun. Biol.* **4**, 874 (2021).

39. J. He, T. Li, S. Y. Huang, Improvement of cryo-EM maps by simultaneous local and non-local deep learning. *Nat. Commun.* **14**, 3217 (2023).

40. A. W. Senior, R. Evans, J. Jumper, J. Kirkpatrick, L. Sifre, T. Green, C. Qin, A. Zidek, A. W. R. Nelson, A. Bridgland, H. Penedones, S. Petersen, K. Simonyan, S. Crossan, P. Kohli, D. T. Jones, D. Silver, K. Kavukcuoglu, D. Hassabis, Improved protein structure prediction using potentials from deep learning. *Nature* **577**, 706–710 (2020).

41. J. Qin, Z. Wang, M. Hoogeveen-Westerveld, G. Shen, W. Gong, M. Nellist, W. Xu, Structural basis of the interaction between tuberous sclerosis complex 1 (TSC1) and Tre2-Bub2-Cdc16 domain family member 7 (TBC1D7). *J. Biol. Chem.* **291**, 8591–8601 (2016).

42. P. Emsley, K. Cowtan, Coot: Model-building tools for molecular graphics. *Acta Crystallogr. D Biol. Crystallogr.* **60**, 2126–2132 (2004).

43. T. I. Croll, ISOLDE: A physically realistic environment for model building into low-resolution electron-density maps. *Acta Crystallogr. D. Struct. Biol.* **74**, 519–530 (2018).

44. E. F. Pettersen, T. D. Goddard, C. C. Huang, E. C. Meng, G. S. Couch, T. I. Croll, J. H. Morris, T. E. Ferrin, UCSF ChimeraX: Structure visualization for researchers, educators, and developers. *Protein Sci.* **30**, 70–82 (2021).

45. E. F. Pettersen, T. D. Goddard, C. C. Huang, G. S. Couch, D. M. Greenblatt, E. C. Meng, T. E. Ferrin, UCSF Chimera—A visualization system for exploratory research and analysis. *J. Comput. Chem.* **25**, 1605–1612 (2004).

46. D. Aragao, J. Aishima, H. Cherukuvada, R. Clarken, M. Clift, N. P. Cowieson, D. J. Ericsson, C. L. Gee, S. Macedo, N. Mudie, S. Panjikar, J. R. Price, A. Riboldi-Tunnicliffe, R. Rostan, R. Williamson, T. T. Caradoc-Davies, MX2: A high-flux undulator microfocus beamline serving both the chemical and macromolecular crystallography communities at the Australian Synchrotron. *J. Synchrotron Radiat.* **25**, 885–891 (2018).

47. W. Kabsch, Xds. *Acta Crystallogr. D Biol. Crystallogr.* **66**, 125–132 (2010).

48. M. D. Winn, C. C. Ballard, K. D. Cowtan, E. J. Dodson, P. Emsley, P. R. Evans, R. M. Keegan, E. B. Krissinel, A. G. Leslie, A. McCoy, S. J. McNicholas, G. N. Murshudov, N. S. Pannu, E. A. Potterton, H. R. Powell, R. J. Read, A. Vagin, K. S. Wilson, Overview of the CCP4 suite and current developments. *Acta Crystallogr. D Biol. Crystallogr.* **67**, 235–242 (2011).

49. P. A. Karplus, K. Diederichs, Linking crystallographic model and data quality. *Science* **336**, 1030–1033 (2012).

50. P. D. Adams, P. V. Afonine, G. Bunkoczi, V. B. Chen, I. W. Davis, N. Echols, J. J. Headd, L. W. Hung, G. J. Kapral, R. W. Grosse-Kunstleve, A. J. McCoy, N. W. Moriarty, R. Oeffner, R. J. Read, D. C. Richardson, J. S. Richardson, T. C. Terwilliger, P. H. Zwart, PHENIX: A comprehensive Python-based system for macromolecular structure solution. *Acta Crystallogr. D Biol. Crystallogr.* **66**, 213–221 (2010).

51. P. Emsley, Tools for ligand validation in Coot. *Acta Crystallogr. D. Struct. Biol.* **73**, 203–210 (2017).

52. C. J. Williams, J. J. Headd, N. W. Moriarty, M. G. Prisant, L. L. Videau, L. N. Deis, V. Verma, D. A. Keedy, B. J. Hintze, V. B. Chen, S. Jain, S. M. Lewis, W. B. Arendall III, J. Snoeyink, P. D. Adams, S. C. Lovell, J. S. Richardson, D. C. Richardson, MolProbity: More

and better reference data for improved all-atom structure validation. *Protein Sci.* **27**, 293–315 (2018).

53. B. Yang, Y. J. Wu, M. Zhu, S. B. Fan, J. Lin, K. Zhang, S. Li, H. Chi, Y. X. Li, H. F. Chen, S. K. Luo, Y. H. Ding, L. H. Wang, Z. Hao, L. Y. Xiu, S. Chen, K. Ye, S. M. He, M. Q. Dong, Identification of cross-linked peptides from complex samples. *Nat. Methods* **9**, 904–906 (2012).

54. M. Krzywinski, J. Schein, I. Birol, J. Connors, R. Gascoyne, D. Horsman, S. J. Jones, M. A. Marra, Circos: An information aesthetic for comparative genomics. *Genome Res.* **19**, 1639–1645 (2009).

55. I. Fokkema, M. Kroon, J. A. Lopez Hernandez, D. Asscheman, I. Lugtenburg, J. Hoogenboom, J. T. den Dunnen, The LOVD3 platform: Efficient genome-wide sharing of genetic variants. *Eur. J. Hum. Genet.* **29**, 1796–1803 (2021).

56. J. G. Tate, S. Bamford, H. C. Jubb, Z. Sondka, D. M. Beare, N. Bindal, H. Boutselakis, C. G. Cole, C. Creatore, E. Dawson, P. Fish, B. Harsha, C. Hathaway, S. C. Jupe, C. Y. Kok, K. Noble, L. Ponting, C. C. Ramshaw, C. E. Rye, H. E. Speedy, R. Stefancsik, S. L. Thompson, S. Wang, S. Ward, P. J. Campbell, S. A. Forbes, COSMIC: The catalogue of somatic mutations in cancer. *Nucleic Acids Res.* **47**, D941–D947 (2019).

57. P. D. Stenson, M. Mort, E. V. Ball, K. Evans, M. Hayden, S. Heywood, M. Hussain, A. D. Phillips, D. N. Cooper, The human gene mutation database: Towards a comprehensive repository of inherited mutation data for medical research, genetic diagnosis and next-generation sequencing studies. *Hum. Genet.* **136**, 665–677 (2017).

58. J. Jumper, R. Evans, A. Pritzel, T. Green, M. Figurnov, O. Ronneberger, K. Tunyasuvunakool, R. Bates, A. Zidek, A. Potapenko, A. Bridgland, C. Meyer, S. A. A. Kohl, A. J. Ballard, A. Cowie, B. Romera-Paredes, S. Nikolov, R. Jain, J. Adler, T. Back, S. Petersen, D. Reiman, E. Clancy, M. Zielinski, M. Steinegger, M. Pacholska, T. Berghammer, S. Bodenstein, D. Silver, O. Vinyals, A. W. Senior, K. Kavukcuoglu, P. Kohli, D. Hassabis, Highly accurate protein structure prediction with AlphaFold. *Nature* **596**, 583–589 (2021).

59. A. Punjani, D. J. Fleet, 3D variability analysis: Resolving continuous flexibility and discreteheterogeneity from single particle cryo-EM. *J. Struct. Biol.* **213**, 107702 (2021).

60. A. S. I. Cook, J. H. Hurley, Toward a standard model for autophagosome biogenesis. *J. Cell Biol.* **222**, e202304011 (2023).